Earth Syst. Dynam. Discuss., 5, 1275–1317, 2014
www.earth-syst-dynam-discuss.net/5/1275/2014/
doi:10.5194/esdd-5-1275-2014

Earth System Dynamics Discussions
Open Access

Large scale atmospheric forcing and topographic modification of precipitation rates over High Asia – a neural network based approach

L. Gerlitz, O. Conrad, and J. Böhner

University of Hamburg, Institute of Geography, Bundesstraße 55, 20146 Hamburg, Germany

Received: 29 August 2014 – Accepted: 12 September 2014 – Published: 13 October 2014

Correspondence to: L. Gerlitz (lars.gerlitz@uni-hamburg.de)

Published by Copernicus Publications on behalf of the European Geosciences Union.

Abstract

The heterogeneity of precipitation rates in high mountain regions is not sufficiently captured by state of the art climate reanalysis products due to their limited spatial resolution. Thus there exists a large gap between the available data sets and the demands of climate impact studies. The presented approach aims to generate spatially high resolution precipitation fields for a target area in Central Asia, covering the Tibetan Plateau, the adjacent mountain ranges and lowlands. Based on the assumption, that observed local scale precipitation amounts are triggered by varying large scale atmospheric situations and modified by local scale topographic characteristics, the statistical downscaling approach estimates local scale precipitation rates as a function of large scale atmospheric conditions, derived from the ERA-Interim reanalysis, and high resolution terrain parameters. Since the relationships of the predictor variables with local scale observations are rather unknown and highly non-linear, an Artificial Neural Network (ANN) was utilized for the development of adequate transfer functions. Different ANN-architectures were evaluated with regard to their predictive performance.

The final downscaling model was used for the cellwise estimation of monthly precipitation sums, the number of rainy days and the maximum daily precipitation amount with a spatial resolution of 1 km^2. The model was found to sufficiently capture the temporal and spatial variations of precipitation rates in the highly structured target area and allows a detailed analysis of the precipitation distribution. A concluding sensitivity analysis of the ANN model reveals the effect of the atmospheric and topographic predictor variables on the precipitation estimations in the climatically diverse subregions.

1 Introduction

The large scale spatial pattern and the seasonal and interannual variability of precipitation rates over Central and High Asia has been widely studied, particularly with regard to its impact on downstream hydrological regimes and hence on the climate-sensitive

ESDD
5, 1275–1317, 2014

agriculture dominated economies of the highly populated downstream areas (Akhtar et al., 2008; Mall et al., 2006; Matthews et al., 1997). The main rivers of South and East Asia such as Indus, Ganges, Brahmaputra, Huang-He and Yangtze have their upper catchment areas on the Tibetan Plateau or in the adjacent mountain regions and are mainly fed by the enhanced precipitation rates compared with the surrounding lowlands and by snow melting in spring. Glacial runoff contributes to a lesser extent but is crucial for the base flow during dry season (Immerzeel and Bierkens, 2010). The glacial dynamics are likewise distinctly influenced by the local- and mesoscale climate variability (Maussion et al., 2013). For investigation of the various interactions of climate and climate change with the ecosystems of Central and High Asia spatial high resolution climate data are required. While the temporal and spatial variations of near surface temperatures over Central and High Asia have been modeled with reliable results (Böhner, 2006; Gerlitz et al., 2014), the accuracy and spatial resolution of available gridded precipitation estimates do not satisfy the demands of climate impact studies so far (Schoof, 2013). Gridded climate reanalysis products, such as ERA-Interim, adequately simulate the large scale atmospheric features over Asia, but fail to capture the topographic variability of precipitation rates over the highly structured target area. Against this background, we present a rather generic empirical approach, which enables an estimation of local scale monthly precipitation rates, basically merging statistical downscaling of large scale atmospheric fields and DEM-based terrain parameterization methods. Therefore we consider local scale precipitation as a function of large scale atmospheric parameters on the one hand and a local scale terrain induced modification on the other. Selected terrain parameters were developed and evaluated with regard to their representation of the local scale precipitation-genetic processes. Subsequently statistical relationships between large scale atmospheric conditions, terrain parameters and local scale precipitation observations were analyzed and adequate transfer functions were developed. Statistical downscaling approaches aim to identify and quantify a robust relationship between independent large scale atmospheric parameters and the observed local scale weather and to calibrate prognostic

ESDD
5, 1275–1317, 2014

transfer functions for the prediction under altering synoptic conditions. By means of the integration of terrain parameters statistical downscaling can be combined with climate regionalization applications, which allows the assessment of gridded high resolution climate data as function of large scale synoptic parameters and local scale terrain characteristics.

Based on the assumption, that the atmosphere–topography interactions are highly nonlinear, we utilized an artificial neural network (ANN) approach for the analysis of the statistical relationships. Neural networks stand out due to their ability to approximate any continuous multidimensional function and their capability to handle the interactions of interconnected predictors. Particularly for the examination of complex systems with unknown relationships between several predictor and predictant variables, neural networks have been increasingly used in the field of climate- and geoscience. Compared to dynamical downscaling procedures (Dimri et al., 2013; Maussion et al., 2013), statistical approaches are less computer demanding, although a missing physical consistency of statistical downscaling approaches is often criticized. However, Schoof (2013) illustrates, that the results of complex statistical methods often lead to comparable results. Due to the integration of physically based terrain parameters for the estimation of local scale precipitation rates, the presented approach remains physically consistent and can be utilized for the development of local scale climate change scenarios.

In the following section, we first provide a brief overview of large scale circulation modes, associated pluviometric regimes and their topographic modifications over the target area. Subsequently, we introduce the utilized large scale atmospheric data sets and the derivation of precipitation-relevant terrain parameters in Sect. 3.1. Section 3.2 addresses the implementation and validation of the statistical model. Subsequently, the spatio-temporal variability of precipitation rates over the target area as well as the influence of the major atmospheric and topographic predictors is analyzed in Sect. 3.

ESDD
5, 1275–1317, 2014

2 Large scale circulation modes, pluviometric regimes and the role of topography

The target area, shown in Fig. 1 covers the Tibetan Plateau, the main mountain ranges of High Asia, such as the Himalayan Arc, the Kunlun Shan and the Quilian Shan, as well as the adjacent Indus–Ganges Lowlands, the Tarim Basin and the Red Basin. Extending from 80 to 105° E and 25 to 42° N, the pluviometric regimes of this vast area are controlled by both, tropical-subtropical as well as extratropical circulation systems. Seasonal shifts in large-scale circulation modes and the associated alternation of air masses lead to a distinct hygric seasonality commonly subsumed under the term "monsoon". Although this characteristic differentiation between a rather moist summer and a dry winter season is valid for most of the target area, precipitation regimes and its spatial domains differ in terms of air masses and involved synoptic processes. In general, the target area is controlled by three major pluviometric regimes: the East Asian summer monsoon, the South Asian summer monsoon (syn. Indian summer monsoon) and the extratropical westerlies and its associated fronts and disturbances (Böhner, 2006; Maussion et al., 2013).

In summer the continental areas of the target area and especially the elevated Tibetan Plateau act as a heat source, which triggers the development of the autochthonous "plateau monsoon", a shallow direct circulation mode converging above the Tibetan Plateau (Flohn, 1987). Enhanced flux of sensible heat from the elevated heat source and the release of latent heat in high reaching convection clusters over the north-eastern Indian plains and adjacent mountain ranges lead to the formation of a warm anticyclone in the mid to upper troposphere (monsoon high) and establishes the 500–200 hPa layer over southern Tibet as the earth's free-atmosphere warm pole. The resulting reversal of upper-troposphere temperature gradients in the Indian–Indonesian forces the development of the Tropical Easterly Jet, a powerful permanent component of the large-scale summer monsoon system, which controls trajectories of monsoonal disturbances south of the Himalayas tracking from east to west as well

ESDD
5, 1275–1317, 2014

as the alternating formation of convection cells and frontal rains in south-eastern Tibet (Böhner, 2006; Domrös, 1988; Flohn, 1987). Due to lower radiation income and thermal capacity, strong high pressure cells form over the adjacent Indian and Pacific Ocean. Thus the shallow trough over Tibet leads to converging moist air masses over the Asian continent (Maussion et al., 2013). The Himalayan Arc acts as a barrier to the near surface monsoonal currents, which results in an orographic uplift of moist air masses and strong convection over India and the southern slopes of the Himalayas so as to the formation of the monsoon trough over the Indian Lowlands (Böhner, 2006). The main moisture fluxes for the South Asian summer monsoon originate over the Bay of Bengal and lead to intensive and perpetual precipitation over the eastern Indus–Ganges Lowlands and the adjacent mountain ranges. The moist air masses penetrate the meridional Three River Gorges and lead to enhanced precipitation rates in South Eastern Tibet. A minor monsoonal current advects moist air masses from the Arabian Sea into Western India and the Western Himalayas (Sigdel and Ikeda, 2012). Since the western monsoonal current is weaker, a clear east–west gradient of summer precipitation rates over the Indus–Ganges Lowlands and the Himalayan Arc can be observed (Böhner, 2006; Wulf et al., 2010). The Central and Western Tibetan Plateau is less directly influenced by monsoonal air masses. Precipitation events are mainly associated with diurnal local scale convection due to high rates of solar irradiation (Maussion et al., 2013).

The easternmost parts of the investigation area are mainly influenced by the East Asian summer monsoon. The advection of dry continental air from northern directions and the flux of moist tropical air originating from the western Pacific lead to intensive front formation in the middle troposphere of the polar mixing zone. The resulting quasi-stationary fronts and its associated cloud fields and rain regimes cover large domains over East Asia. Particularly at the Mei–Yu front, where oceanic and continental air masses converge, high precipitation rates appear, with highest values in the south eastern part of the study area, particularly at the exposed slopes of the mountain ranges surrounding the Red Basin (Böhner, 2006).

ESDD
5, 1275–1317, 2014

The northern part of the target area remains north of the ITCZ during summer season and hence is mainly influenced by extratropical westerlies. However due to the shadowing effect of the Pamir, Karakoram and Tian Shan mountain ranges (outside of the target area) the Tarim Basin remains dry with summer precipitation rates below 25 mm (Xu et al., 2004). Only the elevated and west exposed regions of the Kunlun and Quilian Shan receive summer precipitation due to western cyclonic activity (Böhner, 2006). During post monsoon season the pressure cells over Asia and the adjacent oceans dissolve and the ITCZ shifts southward. The area influenced by western circulation patterns spreads south and reaches the Himalayan Arc in winter season. The Tibetan Plateau and the continental regions of Central Asia now act as a cold source, resulting in the formation of the Asiatic High over Mongolia and northern China. The associated strong pressure gradients between the high pressure cell over Asia and its counterparts, the Aleutian Low over the Pacific Ocean and the ITCZ over the Indian Ocean, lead to a divergent near surface flow over Central and High Asia. Thus the target area is under influence of dry continental air masses. The 200 hPa jetstream at the planetary frontal zone reaches its southernmost position in January at 35° N. Due to the blocking effect of the Tibetan Plateau the jetstream is divided into two branches. While the northern current is situated near the Altai Mountains (north of the target area), the southern branch follows the slopes of the Himalayas. The western Himalayas, particularly west facing slopes, receive a considerable amount of winter precipitation associated with the uplift of the westerly flow and western disturbances brought by the 200 hPa jetstream (Böhner, 2006; Maussion et al., 2013; Wulf et al., 2010). The eastern parts of the study area receive less precipitation due to the shadowing effect of the Tibetan Plateau and the mountain ranges of High Asia. The wintertime precipitation mainly occurs in the higher elevations due to orographic uplift. The Indian plains are under the influence of the subtropical subsiding motion of the Hadley cell and are characterized by stable atmospheric conditions (Böhner, 2006). In spring the pressure gradients over Asia decrease due to increasing solar irradiation. The northern branch of the 200 hPa jetstream strengthens, the major trajectories of the western disturbances

ESDD
5, 1275–1317, 2014

shift northward. The Indus–Ganges Lowlands and especially the southern Himalayan slopes receive high solar radiation, which results in occasional convective precipitation events (Romatschke et al., 2010).

The investigation of the interannual variability of precipitation rates over Central and High Asia often focuses on the summer monsoon season. Most studies (Li and Yanai, 1996; Peings and Douville, 2010; Prodhomme et al., 2014) reveal that the intensity of the monsoon highly depends on the magnitude of pressure gradients. The formation and intensity of the low pressure cell over Asia is mainly triggered by the radiative heating of the Tibetan Plateau. An enhanced snow cover during winter and spring increases the surface albedo and results in a delayed and reduced formation of the thermal low. Related to that, paleoclimatic reconstructions show that cold periods (such as Little Ice Age in the 17th century) are characterized by reduced monsoonal precipitation rates, while warmer periods (e.g. the medieval optimum between the 11th and the 14th century) were found to be considerably wetter (Rehfeld et al., 2013).

Moreover, many studies highlight the importance of the Southern Oscillation for the intensity of monsoonal precipitation (Sankar et al., 2011; Shrestha, 2000), although some studies illustrate, that the correlation of the SOI-Index and the Indian and the East-Asian summer monsoon precipitation weakened during recent decades (Kumar et al., 1999; Wang and He, 2012). During El Nino events the zonal Walker circulation over the Pacific Ocean weakens or turns, leading to subsiding air motions over South East Asia (Pokhrel et al., 2012). Likewise over Central and South Asia, more stable atmospheric conditions were detected during El Nino events, which results in reduced precipitation rates. Sigdel and Ikeda (2012) revealed that particularly the eastern branch of the Indian monsoon weakens during El Nino. This leads to reduced moisture fluxes into the eastern Indus–Ganges Plains and the surrounding mountains. Preethi et al. (2011) point out, that the severe 2009 drought over India was at least partially triggered by a weak El Nino event. The variability of winter precipitation is mainly related to the magnitude of the pressure gradients and the position of the planetary frontal zone and the accompanying westerly jetstream (Dimri et al., 2013).

ESDD
5, 1275–1317, 2014

On the local scale the precipitation distribution over the target area is extremely modified due to the various interactions of moist air masses with complex topography and the accompanying local scale atmospheric processes (Chen et al., 2014; Guan et al., 2009; Suprit and Shankar, 2008). Many studies show, that the elevation plays a crucial role for the precipitation distribution. The near surface monsoonal currents during summer season generate high precipitation rates at the lower elevations, followed by a sharp decrease above 4000 m (Barros et al., 2000; Shrestha et al., 2012). The cyclogenetic winter precipitation reaches higher elevations, due to orographic uplift of the westerly flow. In general the windward slopes receive enhanced precipitation. The orographic precipitation reaches annual amounts of up to 10 000 mm a^{-1} in the Kashi Hills in Northern India. In contrast, the leeward areas of the Trans-Himalaya are characterized by arid conditions even during summer season (Böhner, 2006). Based on the remote sensing derived Tropical Rainfall Measuring Mission (TRMM) Bookhagen and Burbank (2006) show, that the topography of the Southern Himalaya slopes is the main trigger for the local scale precipitation distribution. While the central Himalayas are characterized by a so called one-step-topography, which results in a distinct band of maximal precipitation rates south of the main mountain ranges, the eastern and western parts show a second band of high precipitation at lower elevations due to the orographic barrier of the lesser Himalayas. Likewise the western slopes of the Himalayas, Kunlun and Tian Shan benefit from the westerly flow during winter season (Böhner, 2006; Maussion et al., 2013). The precipitation rates in high mountain regions are further modified by autochthonous local scale circulations, such as the diurnal valley-mountain breeze. The enhanced irradiation at the mountain slopes leads to slope-upward winds and subsiding air motions over the valley bottoms. This results in convection and occasional precipitation events over the slopes, while the valleys remain dry (Böhner and Antonić, 2009).

ESDD
5, 1275–1317, 2014

3 Data and methods

Gridded climate reanalysis products, such as ERA-Interim (developed at the European Center for Medium Range Weather Forecast, ECMWF), simulate 6 hourly large scale atmospheric fields for 60 pressure levels between 1000 and 1 hPa over Asia with a horizontal resolution of 0.7° lat/long (T255) (Berrisford et al., 2009; Dee et al., 2011). Since the ERA-Interim reanalysis combines modeling results with ground and radiosonde observations and remote sensing data using a data assimilation system the free atmospheric fields can be considered as the best guess of the current large scale atmospheric situation for every time step. Many studies reveal that ERA-Interim adequately captures the variability of relevant free air meteorological parameters, even over complex mountain regions (Bao and Zhang, 2012; Gao et al., 2012). Recent evaluations of different reanalysis products show that ERA-Interim has the best accordance with in situ observations derived from near surface meteorological records (Bao and Zhang, 2012) and radiosonde observations over the Tibetan Plateau (Wang and Zeng, 2012) and the Central Himalayan Arc (Jin-Huan et al., 2013). These results were particularly evident for temperature, wind direction and velocity and hydroclimatological parameters. Due to the assimilation of in situ radionsonde and near surface observations we assume that the precipitation relevant moisture fluxes are well represented by ERA-Interim. Sigdel and Ikeda (2012) show that the interannual variability of moisture transports into the target area (e.g. because of variations of the Southern Oscillation) can be captured by reanalysis products. However, their coarse resolution is insufficient to represent the spatial variability of sub-grid atmospheric processes in the highly structured study area. For the analysis of local scale precipitation rates we used daily observations from 157 meteorological stations for the period from 1989 to 2000. Further 18 station records for the period from 2000 to 2011 were used for the evaluation of the modeling approach (Fig. 1). Thus the validation data set is spatially and temporally independent from the model implementation. The station records for the evaluation procedure were chosen as to represent all major geographic subregions of the target area and their

ESDD
5, 1275–1317, 2014

specific climate characteristics. The observations for China and Tibet were provided by the China Meteorological Administration, the records for Nepal were supplied by the Department of Hydrology and Meteorology, Kathmandu/Nepal. All station records were quality proofed using the Neumann-ratio for annual precipitation sums. Further the cumulative residuals were tested as suggested by Buishand (1982). Records showing significant inhomogeneities on the 99 % level were rejected.

It is highly probable that the precipitation records used for this study were partially employed for the assimilation of the ERA-Interim reanalysis. However, since the presented downscaling approach only utilizes free atmospheric variables (see Sect. 2.1), the assimilation of observations in the reanalysis does not lead to considerable redundancies. The precipitation time series were aggregated to monthly sums. For a rough assessment of the temporal precipitation distribution we used the maximum daily amount as well as the number of rainy days as additional predictant variables.

3.1 Atmospheric and topographic predictors

For the characterization of the large scale atmospheric pressure distribution over Asia a principle component analysis (PCA) of the ERA-Interim 500 hPa geopotential height (GPH) fields was conducted for the macrogeographical region between 50° N and 10° S and 30 and 140° E. This allows the identification of the major spatial modes and the temporal variability of the atmospheric circulation over the target area. The PCA-analysis decomposites the time series of gridded GPH fields to a small number of orthogonal atmospheric patterns (referred to as eigenvectors or Empirical Orthogonal Functions, EOFs) and accompanying uncorrelated time indices (scores) (Hannachi et al., 2006). The atmospheric pattern for every time step can then be described as a linear combination of the EOFs and scores. Typically the major part of the large scale atmospheric variability can be explained by only a small number of EOF-fields (Hannachi et al., 2007). This leads to a reduction of the dimensionality of complex systems and removes internal redundancies. The PCA was conducted based on anomalies of the 500 hPa ERA-Interim monthly mean GPH compared with the longtime mean

ESDD
5, 1275–1317, 2014

for the period from 1989 to 2010. For the computation we utilized the package prcomp within the free and Open Source software R. We considered those fields which contribute to more the 1 % of the total variance of the spatio-temporal GPH distribution. Since the position of the major pressure cells over Asia and the adjacent oceans determines the prevailing wind directions and the moisture transport into the target area, the EOF-fields are useful to interpret the circulation variability, particularly with regard to its importance for precipitation-genetic processes. The scores indicate the relevance of the EOF patterns for the pressure distribution of each month and were used as large scale predictors for the presented downscaling approach.

Figure 2 shows the major six EOF-fields and the appendent time series of scores, as well as their portion of variance explained. The first EOF indicates the seasonal shift of the ITCZ and the associated north–southern pressure gradient between the Asian continent and the Indian Ocean. During summer the continent is characterized by a thermal low pressure cell, which results in an uplift of the 500 hPa GPH. At the same time the Indian Ocean is under influence of the southern branch of the Hadley cell, which results in higher sea level pressure and a decrease of the 500 hPa level GPH. In winter season the large scale atmospheric conditions turn due to the southward shift of the ITCZ. The scores of the first EOF show a clear annual cycle, the summer circulation pattern is characterized by positive, the winter pattern by negative scores. The second EOF field addresses a pressure gradient from east to west over the Asian continent. Again the scores suggest an annual cycle of the second EOF, with mainly positive values during summer and negative values during winter season. This is attributed to the formation of a thermal low pressure cell over Central Asia during summer. However the time series of scores show an interannual variability, which is significantly correlated with the index of the Southern Oscillation, defined as SOI $= \frac{\Delta P - \Delta P_{\mathrm{avg}}}{s_{\Delta P}}$, where ΔP indicates the sea level pressure difference between Tahiti and Darwin. ΔP_{avg} is the mean pressure difference and $s_{\Delta P}$ is the accompanying SD ($r = -0.51$, $p = 0.99$). Particularly the extreme 1997/1998 El-Nino event is clearly evident in the time series of EOF-scores (Kirono et al., 1999; Slingo and Annamalai, 2000; Wang et al., 2002). The

ESDD
5, 1275–1317, 2014

first two EOFs already contribute to 84.1 % of the temporal large scale variability of the GPH over the selected region. The third EOF-field (which explains additional 4.4 % of the GPH variability) indicates an uplift and lowering of the 500 hPa level over Northern India and South East Asia.

This band coincidences with the position of the Tropical Easterly Jet during summer season and the trajectories of tropical disturbances (Parth Sarthi et al., 2014).

The fourth EOF pattern addresses an east–west oriented pressure gradient over the Indian Ocean. Pattern five alludes to variations of the 500 hPa level GPH over the Southern Indian Ocean, pattern six indicates variations of the simultaneous formation of pressure cells over the Arabian Sea and the Australian continent. The EOF-fields four to six, however, contribute to less than 2 % of the temporal variability of the 500 hPa level GPH.

For the characterization of precipitation relevant synoptic situations we further processed the ERA-Interim monthly means of relative humidity at the 500 and 200 hPa level. These fields were resampled to a grid size 1 km^2 using thin plate spline and were extracted for every single meteorological station. Many studies (Corbosiero and Molinari, 2002; Frank and Ritchie, 2001; Wingo and Cecil, 2009) mention the vertical wind shear between the 500 and 200 hPa level as an important factor for the spatial and temporal precipitation distribution, particularly with regard to tropical disturbances. Thus the wind shear was derived from the ERA-Interim reanalysis and likewise resampled to the required resolution of 1 km^2.

For the analysis of interactions between the large scale synoptic situation and the varying topographic settings of the target area, terrain parameters were integrated into the downscaling approach. These were derived from the SRTM digital elevation model (Farr et al., 2007) and aggregated to a 1 km^2 resolution. Primary the raw surface elevation (Z) controls the precipitation distribution in complex terrain (Daly et al., 1994). The vertical precipitation gradient however highly depends on the current synoptic conditions. While the monsoonal flow during summer leads to high precipitation rates up to an elevation of 4000 m and a sharp decrease above (Barros et al., 2000), the

ESDD
5, 1275–1317, 2014

cyclogenetic wintertime precipitation reaches higher elevations. The vertical precipitation gradient in mountainous regions is often exaggerated due to the diurnal mountain-valley circulation and the associated convection at the mountain slopes. To account for the spatial variations of terrain induced convection, we utilized the relative elevation above the channel network (Z_{rel}) as an additional predictor variable. Therefore the channel lines were identified and interpolated for the target domain. The elevation above channel line is subsequently calculated as a difference of the surface elevation and the interpolated channel altitudes. The methods for the derivation of the relative elevation above the channel network are available as a complete tool in the free and Open Source Geographical Information System SAGA (Böhner and Antonić, 2009).

Orographic precipitation, resulting from the uplift of moisture-bearing air masses at windward slopes of topographic barriers, and the related leeward rain shadow is probably the most prominent feature of the spatial precipitation distribution in the target area. Based on the assumption, that the windward impact on the precipitation intensity depends on the prevailing large scale wind direction and on the elevation of the orographic barrier, a windward-index (as suggested by Böhner and Antonić, 2009) was used for the presented study. For the Tibetan Plateau with its mean elevation between 4000 and 5000 m, the 500 hPa wind field can be considered as near surface, but also the wind and leeward effects of the major mountain ranges influence the 500 hPa level wind field. Thus we resampled the monthly mean ERA-Interim 500 hPa wind fields to the target resolution of 1 km^2 and subsequently derived the windward and leeward positions. For every grid cell the wind trajectories were followed and the weighted vertical angles of the flow currents were analyzed using the following formulas.

ESDD
5, 1275–1317, 2014

The windward index H_W and the leeward index H_L were calculated to:

$$H_W = \frac{\sum_{i=1}^{n} \frac{1}{d_{WHi}} \cdot \tan^{-1}\left(\frac{d_{WZi}}{d_{WHi}}\right)}{\sum_{i=1}^{n} \frac{1}{d_{LHi}}} + \frac{\sum_{i=1}^{n} \frac{1}{d_{LHi}} \cdot \tan^{-1}\left(\frac{d_{LZi}}{d_{LHi}}\right)}{\sum_{i=1}^{n} \frac{1}{d_{LHi}}} \quad (1)$$

$$H_L = \frac{\sum_{i=1}^{n} \frac{1}{\ln(d_{WHi})} \cdot \tan^{-1}\left(\frac{d_{LZi}}{d_{WHi}}\right)}{\sum_{i=1}^{n} \frac{1}{\ln(d_{LHi})}} \quad (2)$$

were d_{WHi} and d_{LHi} refere to the horizontal distances in windward and lee direction and d_{WZi} and d_{LZi} are the corresponding vertical distances compared with the considered raster cell. The second summand in Eq. (1) accounts for the leeward impact of previously traversed mountain chains. The logarithmized horizontal distances in Eq. (2) lead to a longer distance impact of leeward rain shadow. The final wind effect parameter, which is supposed to be related with the interaction of the large scale wind field and the local scale precipitation characteristics, is calculated to $H = H_L \cdot H_W$ and takes values between 0.7 for leeward and 1.3 for windward positions (Böhner and Antonić, 2009). The cellwise calculation of the wind effect is likewise fully implemented in SAGA-GIS.

Figure 3 shows the spatial distribution of the wind effect as well as the mean 500 hPa wind field exemplarily for January and July 2010. The upper picture shows the complete target area, the lower one is an enlargement of the Central Himalayan Arc. The winter situation is characterized by a homogenous westerly flow which results in high values of the wind effect parameter on the western slopes, particularly at the margins of the Kunlun Shan, Quilian Shan and the Himalayas. During summer the thermal low over the Tibetan Plateau is fully established, resulting in a converging flow pattern at the 500 hPa level. The north-westerly monsoonal currents over Southern Asia lead to maximal values of the wind effect parameter at the southern Himalayan slopes. Especially the first mountain ranges north of the Nepalese border and the major Himalayan peaks are characterized by strong windward positions. In contrast the east–west oriented valleys of Central Nepal are located in the rain shadow of the lower Himalayas.

ESDD
5, 1275–1317, 2014

The strong leeward position of the Trans-Himalayan valleys north of the major peaks is particularly well captured by the spatial distribution of the wind effect parameter.

To account for varying interactions of large scale atmospheric processes and topographic characteristics in the versatile subregions of the target area the geographical coordinates (lat./long.) were considered as further explanatory variables for the presented downscaling approach.

Finally all predictor and predictant variables were normalized by subtracting the mean values and dividing by the corresponding standard deviation.

3.2 Implementation and evaluation of an ANN-model

Traditional statistical methods, most notably linear models, have been frequently used for the quantification of statistical relationships and the implementation of transfer functions (e.g. Böhner, 2006) although the actual predictor–predictant relations are often highly non-linear (Gerlitz, 2014; Sauter and Venema, 2011). Further the data sets used often violate the statistical conditions, e.g. in case of intercorrelated predictor variables or non-normal and non-homogenous residuals (Schönwiese et al., 2010; Schoof and Pryor, 2001). During the last decade complex machine learning algorithms such as Artificial Neural Networks became more prominent in the field of geoscientific research and have been utilized e.g. for hydrological simulations (Dawson and Wilby, 2001; Jain and Kumar, 2007), snow cover prediction (Sauter and Venema, 2011) and habitat modeling (Özesmi and Özesmi, 1999), but also for statistical downscaling and climate modeling applications. For the analysis and prediction of the variability and change of monsoonal precipitation rates over India various recent studies applied ANNs with reliable results (Chattopadhyay, 2007; Shukla et al., 2011; Singh and Borah, 2013). In the field of precipitation downscaling ANNs were utilized (amongst others) by Coulibaly et al. (2005), Dibike and Coulibaly (2006), Mekanik et al. (2013) and Tomassetti et al. (2009). All studies highlight the complexity and non-linearity of the climate system with particular regard to precipitation-genetic processes. A comprehensive review of studies on rainfall prediction based on neural network applications is given by Ranjan Nayak

ESDD
5, 1275–1317, 2014

et al. (2013). Schoof and Pryor (2001) compared the predictive performances of neural network based downscaling approaches with linear regression based methods and concluded that ANNs superiorly capture complex interactions between the large scale synoptic patterns and local scale observations, although they point out, that the results of precipitation downscaling approaches do not achieve the quality of comparable temperature estimations.

Compared to linear models, ANNs stand out due to their flexibility and their capability to approximate any non-linear continuous function. The data driven non-parametric approach can identify input–output relationships without any prior assumptions and can handle intercorrelated predictor variables, which is advantageous if complex systems are to be analyzed and the specific type of internal relationships and interactions is unknown (Günther and Fritsch, 2010; Sauter et al., 2009). Inspired by our conception of the human brain, ANNs are composed of numerous simple parallel operating processing units (referred to as neurons) and associated weights (synapses). The neurons are generally arranged in layers, starting with the input layer, which contains one neuron for each independent variable x_i, one or more hidden layers with an arbitrary number of neurons for the processing of the data and one output layer, which releases the final modeling results. Since an ANN with one hidden layer can already approximate any continuous differentiable function (Schoof and Pryor, 2001) multilayer ANNs are seldom used for regression applications.

Figure 4 shows exemplarily a neural network architecture with three input variables, one hidden layer with two processing units and one output variable. The input passes the vector of time series of the independent variables to the hidden neurons. These receive a signal, which is determined by the so called integration function net_j, defined as a weighted linear combination of the predictant vectors. To account for non-linearities of the input–output relationships the neurons process the signal by means of the activation function φ, which is usually defined as a sigmoid logistic function, mapping the values of the integration function to a domain $\in [0;1]$. The value 1 refers to a strong effect of the particular linear combination of the input vectors for the output result, while 0

ESDD
5, 1275–1317, 2014

indicates a negligible influence. In the final output layer the activation function is linear. For the calculation of the output o_j of any neuron j, the activation function is applied to the net result of the weighted linear combination net_j.

$$o_j = \varphi(\mathrm{net}_j) \quad \text{with} \quad \mathrm{net}_j = \sum_{i=1}^{n} w_i \cdot x_i \quad \text{and} \quad \varphi = \frac{1}{1 + e^{\mathrm{net}_j}} \tag{3}$$

Most ANNs are constructed using a three layer architecture with only one hidden layer, where the processing of the data is conducted. For the presented study we utilized a Feed-Forward ANN, i.e. the information flow is unidirectional. Each neuron receives signals from all nodes of the previous layer and passes the modified signal to the nodes of the subsequent one. The knowledge of an ANN is comprehended in the weights of the integration function. These are initially assigned as random values of the normal distribution. The initial network processes the input-vectors based on the integration and activation functions of the internal neurons and passes an output-signal to the final layer. Since the weights are randomly chosen, the output of the ANN model, compared with observed values, is primarily insufficient. Based on a learning sample the weights are subsequently iteratively adjusted with the aim to minimize the error function, defined as the root mean square error of the desired predictant values and the outcome of the ANN model. For the adjustment of weights several supervised learning algorithms were developed, although most ANN applications are based on the so called backpropagation approach (Hecht-Nielsen, 1989). This algorithm calculates the gradient of the error function with regard to modified weights backward in the network and shifts the weights into the opposite direction of the partial derivates based on a default learning rate. The recursive application of the backpropagation procedure ensures the identification of a local minimum of the error function and the corresponding weights. To discover the best neural network for the regression of the local scale precipitation rates as a function of the above mentioned predictor variables we utilized the resilient backpropagation approach, which is fully implemented in the free and open source R-package neural net (Günther and Fritsch, 2010). This algorithm increases the learning

ESDD
5, 1275–1317, 2014

rate, if the direction of the error gradient keeps its sign. If the sign turns, the learning rate is decreased automatically. This leads to an accelerated conversion of the recursive adjustment of weights and avoids that a minimum is missed due to a too large learning rate.

The most obvious degree of freedom of any ANN approach is its architecture, particularly the number of neurons within the hidden layer. Although thumb rules for the best number of neurons have been suggested (Basheer and Hajmeer, 2000), a general rule, defining the best ANN architecture, could not be determined so far. While an ANN model with too many neurons in the hidden layer tends to overfit, which results in a poor predictive performance, an insufficient number of neurons leads to an over-generalization and hence a non-detection of distinct non-linear relationships within the learning sample. The best ANN architecture highly depends on the number of predictor and predictant variables, the number of cases and the type and complexity of the statistical relationship (Sauter et al., 2009). Thus, for the identification of an optimum ANN for the downscaling approach, we tested several ANN architectures with regard to their predictive power. Starting with only one neuron in the hidden layer, the complexity of the network was gradually increased. Due to exponentially increasing computing demands of the learning phase, the maximum of neurons was set to 10. For every number of neurons an ANN was implemented based on the learning sample containing monthly time series of 157 meteorological stations for the period for 1989 to 2000. The vectors of predictor variables were used as input nodes. As output variables the observed monthly precipitation sum, the maximum of daily precipitation and the number of rainy days were chosen. Every ANN realization was used to predict the output variables for the independent evaluation data set, including time series from 18 stations for the period 2001 to 2011 (see white and red dots in Fig. 1). For the evaluation of the model, the mean squared residuals of each station were calculated and normalized using the mean and the standard deviation of the particular record of observations. This enables the comparison of the model quality for stations with varying precipitation amounts. Figure 5 shows the mean squared error (in standard deviations) of the

ESDD
5, 1275–1317, 2014

monthly precipitation sums for each of the evaluation records. The ANN realizations with only a few neurons in the hidden layer show large residuals for some stations. This is due to an extreme overestimation of precipitation rates for the dry regions in the north of the study region (not shown). With increasing complexity the model better captures the diverse climates of the target area and improves the prediction performance for the evaluation data records. The ANN with 8 hidden neurons was found to have the lowest prediction error of the monthly precipitation sums (with values below 0.5 standard deviations for most of the meteorological stations) and hence was used for the cell-wise estimation of precipitation rates in the target area. The analysis of the prediction power for the maximum daily precipitation and the number of rainy days revealed similar results (not shown). For ANN architectures with more than eight hidden neurons the prediction performance of the model decreased considerably. The maps given in Fig. 5 exemplarily show the predicted fields of precipitation sums for the Central Himalayan region for July 2010 based on varying ANN architectures with $N = 1$, $N = 8$ and $N = 10$ hidden neurons. The simple ANN with only one neuron in the hidden layer does not capture the topographically determined precipitation distribution and mainly depicts an elevational gradient of precipitation sums with high values in the Indus–Ganges Lowlands and lower values in the high mountains and on the elevated Tibetan Plateau. In contrast the ANN with 10 hidden neurons clearly overfits the input–output relationships resulting in a rather unrealistic scattered precipitation field, particularly over the highly complex terrain of the southern Himalayan slopes. The precipitation distribution predicted by the "best" ANN architecture with eight hidden neurons depicts two major precipitation bands, one at the first topographic barrier of the outer Himalayas and one at the southern margin of the highest mountain peaks.

These results highly agree with previous studies on the topographically induced distribution of precipitation rates in the target area (Bookhagen and Burbank, 2006; Maussion et al., 2013) and support the reliability of the statistical model. Figure 6 compares the modeled and observed time series of monthly precipitation sums for 18 independent stations. The spatial distribution of precipitation (with annual precipitations

ESDD
5, 1275–1317, 2014

sums ranging from below 50 mm over the Tarim Basin to more than 4000 mm over the monsoonal influenced Himalayan slopes is well simulated by the ANN model. However for the stations at the southern Himalayan slopes, particularly for Jomsom, which is located in the bottom of the deeply carved Kaligandaki valley in central Nepal, the model clearly overestimates the precipitation amounts.

Likewise the monthly precipitation sums for Allahabad, situated in the western Indus–Ganges Lowlands, are considerably overestimated. This is very likely due to an insufficient number of stations at the southern margin of the target area within the learning sample. For all other records the annual precipitation amounts are properly simulated. The temporal variability of monthly precipitation sums, with highest values during summer season is well captured for the complete target area. The interannual variability of precipitation rates is particularly obvious for the monsoon season. The well documented 2009 drought over India and the Himalayas (Preethi et al., 2011) is clearly evident in the observed and modeled time series of precipitation sums for Jomsom, Phidim, Sikta, Allahabad and Tezpur. The locations of Darlag, Darwu and Tuotuohe (all situated at elevated sites on the Tibetan Plateau) and Sikta (at the southern Himalayan slopes) receive a distinct amount of winter precipitation which is in general well captured by the ANN model. The explained variance of the ANN model ranges from approximately 0.5 for the convective dominated stations in the arid landscapes in the north of the study region to considerable 0.75 in the monsoonal influenced areas south and east of the Tibetan Plateau. Based on the gridded modeling results, a more detailed analysis of the temporal and spatial precipitation distribution in the target area and its essential influencing factors is given below.

4 Results

The ANN model was utilized to estimate gridded monthly precipitation sums, the maximum daily precipitation and the number of rainy days for each month with a horizontal resolution of 1 km^2 for the period from 1989 to 2011. The prominent features of the

ESDD
5, 1275–1317, 2014

spatial, seasonal and interannual variability of modeled precipitation rates were analyzed and are highlighted below with emphasis on the winter and summer type circulation. Therefore the mean precipitation sums for January and July are mapped in Fig. 7. To quantify the interannual variability the coefficient of variation, defined as the ratio of the standard deviation by the mean precipitation sum, was calculated cellwise. Further, for a rough estimation of the precipitation intensity and frequency the percentage of the maximum daily precipitation of the monthly precipitation sum is given in Fig. 7. In comparison to linear models, the complex structure of the ANN does not directly reveal physically interpretable input–output relationships. Thus ANNs are often mentioned as Black-Box-models (Schönwiese et al., 2010). For the identification of the particular synoptic and local scale processes leading to a spatial and temporal precipitation variability in the target area, a local sensitivity analysis was conducted for different locations, representing the varying precipitation regimes in the study region. Therefore in each case, one predictor variable was chosen as a running variable – taking values between the 0.1 to 1.0 percentiles of the learning sample, while all other predictors were set to their mean values (which is 0 for the normalized variables). The predicted precipitation amounts display the response of the ANN model to modified values of the considered predictor variable and provide an insight into the internal model structure.

As expected, the simulated large scale precipitation distribution in the target area is mainly determined by the prevailing atmospheric modes. During winter season the circulation pattern is characterized by the Asiatic high in the boundary layer and the southward shift of the 200 hPa jetstream. The target area is mainly dominated by dry conditions. Particularly for the Tarim Basin no January precipitation was predicted for the entire period. Similarly the Lowlands of India and the Red Basin show monthly precipitation sums below 20 mm. The Tibetan Plateau, especially the western part, which is located leeward of the Karakoram and Pamir mountains, receives mean monthly precipitation sums below 30 mm and shows a large interannual variability of precipitation rates ($c_v > 2$). Meanwhile the Kunlun and Quilian mountains act as a barrier to the prevailing westerly flow. The uplift of the advected air masses and the occasional

ESDD
5, 1275–1317, 2014

passage of westerly disturbances result in considerable winter precipitation amounts. For January the mean precipitation sums at the western slopes of the mountain ranges reach more than 50 mm, for the leeward slopes and the valley bottoms less than 20 mm are characteristic. The rainfall occurs reliable and steadily, the interannual variability is small, the low ratio of maximum daily precipitation and the monthly sum indicates a temporally uniform precipitation distribution and the absence of extreme events (see Fig. 7). The maximum of January precipitation occurs at the western margin of the Himalayas due to a stronger southern branch of the 200 hPa jetstream. The windward slopes receive up to 150 mm in average during January. The amounts of winter precipitation at the Himalayan slopes show a clear gradient from west to east. As the Kunlun and Quilian Shan the Western Himalayas are characterized by a comparably low variability of winter precipitation rates.

During spring season the pressure gradients over Asia decrease. The enhanced radiative forcing leads to occasional convective precipitation events, particularly over India and the southern Himalayan Slopes, while the north of target area remains under dry conditions (figure not shown). In July summer type circulation pattern is fully established, the monsoonal flow leads to intense moisture fluxes into the study region. Particularly the Indus–Ganges Lowlands and the Himalayan Slopes receive heavy rainfall with mean monthly sums of more than 1000 mm at windward positions. As observed by Bookhagen and Burbank (2006), the model results indicate the occurrence of two high precipitation bands at the southern Himalayan margin. The first discontinuous zone of high precipitation is located at the windward sites of the first orographic barrier of the outer Himalayas at elevations between 1500 and 2000 m. A second band of high precipitation occurs south of the highest Himalayan peaks at elevations between 2000 and 2500 m. The zones of maximal precipitation are followed by a sharp decrease above 4000 m. The variability of monsoonal precipitation at the Himalayan slope is low, particularly for the eastern Himalayas c_v values below 0.1 were computed by the ANN model. The leeward regions of the Trans-Himalayas receive less than 90 mm average precipitation during July. Contemporaneously the Red Basin is under the influence of

ESDD
5, 1275–1317, 2014

the East-Asian monsoon and receives precipitation amounts of more than 300 mm in average during July. For the windward slopes east of the Tibetan Plateau monthly precipitation sums of up to 1000 mm were estimated. Again the interannual variability of the monsoonal precipitation was found to be low with c_v values below 0.1. The precipitation distribution over the Tibetan Plateau shows a clear east–west gradient during summer season. The east of the Plateau is penetrated by moist monsoonal air masses due to the meridional orientation of the Three River Gorges. This results in monthly precipitation sums of up to 150 mm. The western part is situated leeward of the Himalayan and Karakoram mountain ranges and thus remains under dry conditions. For the valley bottoms the monthly precipitation estimations amount to less than 20 mm, for the elevated sites up to 50 mm were computed. This indicates a rather convective precipitation regime by implication of the diurnal mountain-valley circulation. The interannual variability is remarkable higher compared to advective dominated regions such as the windward slopes of the main mountain ranges ($c_v > 0.4$, see Fig. 7). Likewise the higher ratio of maximum daily precipitation and the monthly precipitation sum (partially 40 % of the monthly precipitation amount fall within one day) indicates the occurrence sporadic precipitation events. The Quilian mountains receive higher summer precipitation amounts of more than 70 mm during July and mark the border of the East-Asian monsoonal influence. The leeward slopes, the Tsaidam Depression in the south-east of the Quilian Shan, and the Tarim Basin are characterized by mean monthly precipitation sums below 20 mm and a considerable larger interannual variability with c_v values ranging from 0.3 to 0.5. In the Tarim Basin the maximum of daily precipitation exceeds 50 % of the monthly precipitation sum. This indicates the importance of autochthonous convective precipitation events for the northernmost part of the study region.

The estimated mean annual precipitation sums (figure not shown) reach 1500 to 2000 mm in the Lowlands of India and more than 4000 mm at the southern slopes of the Central Himalayas. The Indian Lowlands and the eastern Himalayas receive more than 80 % of the annual rainfall during summer season. For the western Himalayas the percentage of summer precipitation reaches barely 60 % of the annual amount.

ESDD
5, 1275–1317, 2014

The annual precipitation estimates for the Tibetan Plateau reveal a strong east–west gradient with amounts below 100 mm in the far west and above 1000 mm in the monsoonal influenced eastern part. Particularly in Western Tibet the valley bottoms are characterized by arid conditions with annual precipitation sums below 100 mm, while the elevated sites reach values of up to 350 mm. The precipitation estimates for the Kunlun mountains amount to approximately 400 to 600 mm with maximum values in the far west due to an enhanced winter precipitation (DJF), which reaches up to 50 % of the annual precipitation sum. The annual precipitation over the Qulian Shan reaches 500 to 600 mm with highest values at the stronger monsoonal influenced eastfacing slopes. The Tarim Basin is characterized by dry conditions throughout the year, the annual precipitation sum amounts to less than 80 mm. The convective precipitation during summer season amounts to almost 90 % of the annual sum.

A sensitivity analysis was conducted for the locations of meteorological stations used for the evaluation of the ANN model. The results are exemplarily illustrated for four locations, representing the large scale climatic heterogeneity of the target area. The ANN signal of each predictor variable for the monthly precipitation sums and the maximum daily precipitation amount is plotted in Fig. 8. The station Sikta, situated near the Southern Nepali border, represents the monsoonal climate of the Indian Lowlands and the slopes of the Himalayas. The first EOF (indicating the pressure gradient between the Asian continent and the Indian Ocean) and the relative humidity (especially at 200 hPa) were found to be the crucial large scale predictors for the observed precipitation rates. A strong positive pressure gradient during summer season intensifies the monsoonal circulation and leads to enhanced precipitation rates over the Indus–Ganges Lowlands and the Himalayan Arc. The positive response to increasing values of second EOF scores (which are negatively correlated with the SOI-Index) indicates a positive implication of El-Nino events for the monsoonal precipitation amounts at first sight. However a further correlation analysis of the predictor variables reveals a strong negative relationship ($r > 0.5$, $p = 0.95$) of the EOF2-scores and the 500 hPa relative humidity during summer season for all stations located in the Indian Lowlands and at the southern

ESDD
5, 1275–1317, 2014

Himalayan slopes. For other regions of the target area, no significant correlation could be identified. This indicates a decreased moisture flux into the target area during El-Nino events, which is sufficiently captured by the assimilated ERA-Interim reanalysis. Particularly for the 2009 monsoon season the relative humidity fields of the reanalysis show a considerable negative anomaly over India and the Himalayas (not shown). In combination with a slight negative anomaly of the large scale pressure gradients, this results in reduced precipitation rates predicted by the ANN model (see Fig. 6). The negative response to increasing values of the wind shear has to be interpreted with regard to the annual shift of the 200 hPa jetstream. While the windshear over India during monsoon season is comparably low, the winter circulation pattern is characterized by high wind speeds in the upper troposphere. Although southward shift of the jetstream leads to the occasional passage of westerly disturbances, the winter season is mainly dominated by dry synoptic conditions. For the local scale precipitation distribution the wind effect parameter could be identified as the major topographic predictor variable for the Himalayan slopes, resulting in a considerable topographic differentiation of the precipitation estimates. The negative response of increasing elevations implies the sharp precipitation decrease above 4000 m. The sensitivity analysis for Darwu (located on the eastern Tibetan Plateau) shows a similar response for most of the synoptic and topographic predictor variables. However, in comparison to the southern Himalayan slopes, the precipitation estimates show a clear positive response to increasing values of the relative elevation above the nearest channel network. Particularly for the maximum daily precipitation amounts the response of the ANN model to variations of Z_{rel} was found to be considerably larger than the influence of the wind effect. This indicates the importance of convective precipitation events for the spatial precipitation distribution over the eastern Tibetan Plateau and especially for the generation of intense precipitation events. For the location of Xainza (Western Plateau) the ANN response to variations of the wind effect seems to be negligible. Elevation and relative elevation above the channel network were detected as the most influential predictors for the spatial precipitation distribution, indicating a rather convective precipitation regime over

ESDD
5, 1275–1317, 2014

the Western Tibetan Plateau. The precipitation distribution over the homogenous Tarim Basin (represented by the location of Alar) appears to be rather unaffected by varying topographic settings. The ANN model mainly responses to variations of the moisture fluxes into the Tarim basin, represented by the 500 hPa relative humidity of the ERA-Interim reanalysis. A slight positive response to increased EOF1-scores is most likely due to isochronous development of the summer monsoon circulation pattern and the occurrence of convective precipitation events and should not be interpreted as a monsoonal influence.

5 Conclusions and outlook

The presented ANN downscaling approach sufficiently captures the large and local scale variations of the precipitation distribution in the highly structured target area. By means of the integration of physically based terrain parameters, the approach addresses particular local scale atmospheric processes and remains physically consistent.

Especially for the monsoonal dominated precipitation regimes of the Indus–Ganges Lowlands, the Himalayan slopes and the Red Basin the approach explains up to 70 % of the variability of monthly precipitation sums. However for the Kunlun and Quilian mountains, where precipitation occurs mainly due to western circulation patterns, and for the convective dominated regions, such as the Western Tibetan Plateau and the Tarim Basin, the results are less reliable ($r^2 = 0.5$).

The trained ANN model stands out due to its non-linearity and its ability to capture the interactions of related large scale atmospheric and topographic predictor variables and satisfactorily estimates the net effect for the precipitation predictions. A subsequent local sensitivity analysis can reveal the influence of distinct predictor variables to the ANN output. While the large scale spatial variations and the seasonal cycle of the monthly precipitation amounts were found to be determined by varying circulation modes and moisture fluxes, as represented by the ERA-Interim reanalysis, the

ESDD
5, 1275–1317, 2014

local scale precipitation distribution was found to be highly influenced by topographic characteristics. However the impact of the topographic parameters highly depends on the large scale climatic regimes. Precisely for that reason complex Artificial neural networks are effective modeling tools, particularly in comparison with linear models, which suggest a constant statistical relationship of predictor and predictant variables for the entire target area. While windward and leeward positions were identified as the major topographic predictor for the local scale spatial precipitation variations in the monsoonal dominated regions of India and the Himalayas, the rather convective dominated precipitation regimes of the Western Tibetan Plateau appear to be mainly influenced by the relative elevation above channel network and the accompanied diurnal mountain-valley circulation.

The spatial resolution of the modeled precipitation rates of 1 km^2 is auspicious for climate impact studies, e.g. for the analysis of climato-sensitive ecosystems and hydrological regimes. However the focus of the presented study on monthly precipitation estimates still does not satisfy the requirements of several geoscientific modeling approaches. Hence further research needs to be done to generate spatial and temporal high resolution precipitation estimates. Since the terrain induced precipitation-genetic processes show a large temporal variability due to varying mesoscale atmospheric characteristics, the assessment of daily precipitation rates remains challenging. Böhner (1996) illustrates, that the representation of precipitation amounts for monthly observations in Central Asia remains below 200 km. This is particularly valid for the convective dominated regions of the target area and indicates the heterogeneity of precipitation observations in complex terrain. The daily precipitation amounts in the study region are determined by mesoscale atmospheric processes, such as the passage of tropical and westerly disturbances or the development of convective clusters, which are not sufficiently represented by limited resolution climate models or reanalysis products. The mesoscale atmospheric patterns however are crucial for the identification of the flow direction and the moisture fluxes on a daily time scale. This further increases atmospheric heterogeneity in mountainous regions and impedes the statistical analysis of

ESDD
5, 1275–1317, 2014

interactions between the atmospheric circulation and the underlying topographic characteristics. State of the art dynamical downscaling models can be effective alternatives for the simulation of mesoscale atmospheric processes, but due to their high computational demands and their requirements for high quality input data, most studies focus on a limited spatial domain or time frame. So far the WRF-based High Asian reanalysis (Maussion et al., 2013) is the only data set known to the authors, which adequately captures the mesoscale climatic variability for the entire target region of this study for the reasonable period from 2001 to 2011. However the resolution of 10 km still does not satisfy the needs of many climate impact investigations. The combination of dynamical downscaling and a the presented statistical approach appears to be auspicious for the analysis of mesoscale atmospheric conditions and its modification due to local scale topographic characteristics and should be considered for further research.

Acknowledgements. The ERA-Interim reanalysis fields were freely provided by the ECMWF. We appreciate the supply of daily meteorological observations by the Department of Hydrology and Meteorology (Kathmandu, Nepal) and the Chinese Meteorological Administration (Beijing, China). The study was funded by the Federal Ministry of Education and Research (Berlin, Germany) in the context of the Project CLASH (Climate variability and landscape dynamics in Southeast-Tibet and the eastern Himalaya during the late Holocene reconstructed from tree rings, soils and climate modeling).

References

Akhtar, M., Ahmad, N., and Booij, M. J.: The impact of climate change on the water resources of Hindukush–Karakorum–Himalaya region under different glacier coverage scenarios, J. Hydrol., 355, 148–163, doi:10.1016/j.jhydrol.2008.03.015, 2008.

Bao, X. and Zhang, F.: Evaluation of NCEP/CFSR, NCEP/NCAR, ERA-Interim and ERA-40 reanalysis datasets against independent sounding observations over the Tibetan Plateau, J. Climate, 26, 206–214, doi:10.1175/JCLI-D-12-00056.1, 2012.

ESDD
5, 1275–1317, 2014

Barros, A. P., Joshi, M., Putkonen, J., and Burbank, D. W.: A study of the 1999 monsoon rainfall in a mountainous region in central Nepal using TRMM products and rain gauge observations, Geophys. Res. Lett., 27, 3683–3686, doi:10.1029/2000GL011827, 2000.

Basheer, I. A. and Hajmeer, M.: Artificial neural networks: fundamentals, computing, design, and application, J. Microbiol. Meth., 43, 3–31, 2000.

Berrisford, P., Dee, D., Fielding, K., Fuentes, M., Kallberg, P., Kobayashi, S., and Uppala, S.: The ERA-Interim Archive, ERA Report Series, available at: http://old.ecmwf.int/publications/library/ecpublications/_pdf/era/era_report_series/RS_1.pdf (last access: 15 January 2013), 2009.

Böhner, J.: Säkulare Klimaschwankungen und rezente Klimatrends Zentral- und Hochasiens, Goltze, Göttingen, 1996.

Böhner, J.: General climatic controls and topoclimatic variations in Central and High Asia, Boreas, 35, 279–295, doi:10.1111/j.1502-3885.2006.tb01158.x, 2006.

Böhner, J. and Antonić, O.: Land–surface parameters specific to topo-climatology, in: Developments in Soil Science, vol. 33, chap. 8, Elsevier, Amsterdam, 195–226, 2009.

Bookhagen, B. and Burbank, D. W.: Topography, relief, and TRMM-derived rainfall variations along the Himalaya, Geophys. Res. Lett., 33, L08405, doi:10.1029/2006GL026037, 2006.

Buishand, T. A.: Some methods for testing the homogeneity of rainfall records, J. Hydrol., 58, 11–27, 1982.

Chattopadhyay, S.: Feed forward Artificial Neural Network model to predict the average summer-monsoon rainfall in India, Acta Geophys., 55, 369–382, doi:10.2478/s11600-007-0020-8, 2007.

Chen, F., Liu, Y., Liu, Q., and Li, X.: Spatial downscaling of TRMM 3B43 precipitation considering spatial heterogeneity, Int. J. Remote Sens., 35, 3074–3093, doi:10.1080/01431161.2014.902550, 2014.

Corbosiero, K. L. and Molinari, J.: The effects of vertical wind shear on the distribution of convection in tropical cyclones, Mon. Weather Rev., 130, 2110–2123, doi:10.1175/1520-0493(2002)130<2110:TEOVWS>2.0.CO;2, 2002.

Coulibaly, P., Dibike, Y. B., and Anctil, F.: Downscaling precipitation and temperature with Temporal Neural Networks, J. Hydrometeorol., 6, 483–496, doi:10.1175/JHM409.1, 2005.

Daly, C., Neilson, R. P., and Phillips, D. L.: A statistical-topographic model for mapping climatological precipitation over mountainous terrain, J. Appl. Meteorol., 33, 140–158, doi:10.1175/1520-0450(1994)033<0140:ASTMFM>2.0.CO;2, 1994.

ESDD
5, 1275–1317, 2014

Dawson, C. W. and Wilby, R. L.: Hydrological modelling using artificial neural networks, Prog. Phys. Geogr., 25, 80–108, doi:10.1177/030913330102500104, 2001.
Dee, D. P., Uppala, S. M., Simmons, A. J., Berrisford, P., Poli, P., Kobayashi, S., Andrae, U., Balmaseda, M. A., Balsamo, G., and Bauer, P.: The ERA-Interim reanalysis: configuration and performance of the data assimilation system, Q. J. Roy. Meteorol. Soc., 137, 553–597, 2011.
Dibike, Y. B. and Coulibaly, P.: Temporal neural networks for downscaling climate variability and extremes, Neural Networks, 19, 135–144, doi:10.1016/j.neunet.2006.01.003, 2006.
Dimri, A. P., Yasunari, T., Wiltshire, A., Kumar, P., Mathison, C., Ridley, J., and Jacob, D.: Application of regional climate models to the Indian winter monsoon over the western Himalayas, Sci. Total Environ., 468–469, 36–47, doi:10.1016/j.scitotenv.2013.01.040, 2013.
Domrös, M.: The Climate of China, Springer, Berlin, 1988.
Farr, T. G., Rosen, P. A., Caro, E., Crippen, R., Duren, R., Hensley, S., Kobrick, M., Paller, M., Rodriguez, E., and Roth, L.: The shuttle radar topography mission, Rev. Geophys., 45, RG2004, doi:10.1029/2005RG000183, 2007.
Flohn, H.: Recent investigations on the climatogenetic role of the Quinghai-Xizang Plateau: now and during the Late Cenozoic, in: Reports on the Northeastern Part of the Qighai-Xizang Plateau, edited by: Hovermann, J. and Wenying, W., Lubrecht & Cramer Ltd., Beijing, 1987.
Frank, W. M. and Ritchie, E. A.: Effects of vertical wind shear on the intensity and structure of numerically simulated hurricanes, Mon. Weather Rev., 129, 2249–2269, doi:10.1175/1520-0493(2001)129<2249:EOVWSO>2.0.CO;2, 2001.
Gao, L., Bernhardt, M., and Schulz, K.: Elevation correction of ERA-Interim temperature data in complex terrain, Hydrol. Earth Syst. Sci., 16, 4661–4673, doi:10.5194/hess-16-4661-2012, 2012.
Gerlitz, L.: Using fuzzyfied regression trees for statistical downscaling and regionalization of near surface temperatures in complex terrain, Theor. Appl. Climatol., doi:10.1007/s00704-014-1285-x, in press, 2014.
Gerlitz, L., Conrad, O., Thomas, A., and Böhner, J.: Warming patterns over the Tibetan Plateau and adjacent lowlands derived from elevation- and bias-corrected ERA-Interim data, Clim. Res., 58, 235–246, doi:10.3354/cr01193, 2014.

ESDD
5, 1275–1317, 2014

Guan, H., Hsu, H.-H., Makhnin, O., Xie, H., and Wilson, J. L.: Examination of selected atmospheric and orographic effects on monthly precipitation of Taiwan using the ASOADeK model, Int. J. Climatol., 29, 1171–1181, doi:10.1002/joc.1762, 2009.
Günther, F. and Fritsch, S.: neuralnet: training of neural networks, R Journal, 2, 30–38, 2010.
Hannachi, A., Jolliffe, I. T., Stephenson, D. B., and Trendafilov, N.: In search of simple structures in climate: simplifying EOFs, Int. J. Climatol., 26, 7–28, doi:10.1002/joc.1243, 2006.
Hannachi, A., Jolliffe, I. T., and Stephenson, D. B.: Empirical orthogonal functions and related techniques in atmospheric science: a review, Int. J. Climatol., 27, 1119–1152, doi:10.1002/joc.1499, 2007.
Hecht-Nielsen, R.: Theory of the Backpropagation Neural Network, International Joint Conference on Neural Networks, Washington, D.C., USA, 593–605, 1989.
Immerzeel, W. W. and Bierkens, M. F. P.: Seasonal prediction of monsoon rainfall in three Asian river basins: the importance of snow cover on the Tibetan Plateau, Int. J. Climatol., 30, 1835–1842, doi:10.1002/joc.2033, 2010.
Jain, A. and Kumar, A. M.: Hybrid neural network models for hydrologic time series forecasting, Appl. Soft. Comput., 7, 585–592, doi:10.1016/j.asoc.2006.03.002, 2007.
Jin-Huan, Z. H. U., Shu-Po, M. A., Han, Z. O. U., Li-Bo, Z., and Peng, L. I.: Evaluation of reanalysis products with in situ GPS sounding observations in the Eastern Himalayas, Atmos. Ocean. Sci. Lett., 7, 17–22, 2013.
Kirono, D. G. C., Tapper, N. J., and McBride, J. L.: Documenting Indonesian rainfall in the 1997/1998 El Niño event, Phys. Geogr., 20, 422–435, doi:10.1080/02723646.1999, 1999.
Kumar, K., Rajagopalan, B., and Cane, M.: On the weakening relationship between the indian monsoon and ENSO, Science, 284, 2156–2159, 1999.
Li, C. and Yanai, M.: The onset and interannual variability of the Asian summer monsoon in relation to land–sea thermal contrast, J. Climate, 9, 358–375, doi:10.1175/1520-0442(1996)009<0358:TOAIVO>2.0.CO;2, 1996.
Mall, R. K., Singh, R., Gupta, A., Srinivasan, G., and Rathore, L. S.: Impact of climate change on Indian agriculture: a review, Climatic Change, 78, 445–478, doi:10.1007/s10584-005-9042-x, 2006.
Matthews, R. B., Kropff, M. J., Horie, T., and Bachelet, D.: Simulating the impact of climate change on rice production in Asia and evaluating options for adaptation, Agr. Syst., 54, 399–425, doi:10.1016/S0308-521X(95)00060-I, 1997.

ESDD
5, 1275–1317, 2014

Maussion, F., Scherer, D., Mölg, T., Collier, E., Curio, J., and Finkelnburg, R.: Precipitation seasonality and variability over the Tibetan Plateau as resolved by the High Asia Reanalysis*, J. Climate, 27, 1910–1927, doi:10.1175/JCLI-D-13-00282.1, 2013.

Mekanik, F., Imteaz, M. A., Gato-Trinidad, S., and Elmahdi, A.: Multiple regression and Artificial Neural Network for long-term rainfall forecasting using large scale climate modes, J. Hydrol., 503, 11–21, doi:10.1016/j.jhydrol.2013.08.035, 2013.

Özesmi, S. L. and Özesmi, U.: An artificial neural network approach to spatial habitat modelling with interspecific interaction, Ecol. Model., 116, 15–31, doi:10.1016/S0304-3800(98)00149-5, 1999.

Parth Sarthi, P., Agrawal, A., and Rana, A.: Possible future changes in cyclonic storms in the Bay of Bengal, India under warmer climate, Int. J. Climatol., doi:10.1002/joc.4053, in press, 2014.

Peings, Y. and Douville, H.: Influence of the Eurasian snow cover on the Indian summer monsoon variability in observed climatologies and CMIP3 simulations, Clim. Dynam., 34, 643–660, doi:10.1007/s00382-009-0565-0, 2010.

Pokhrel, S., Chaudhari, H. S., Saha, S. K., Dhakate, A., Yadav, R. K., Salunke, K., Mahapatra, S., and Rao, S. A.: ENSO, IOD and Indian summer monsoon in NCEP climate forecast system, Clim. Dynam., 39, 2143–2165, doi:10.1007/s00382-012-1349-5, 2012.

Preethi, B., Revadekar, J. V., and Kripalani, R. H.: Anomalous behaviour of the Indian summer monsoon 2009, J. Earth Syst. Sci., 120, 783–794, doi:10.1007/s12040-011-0112-3, 2011.

Prodhomme, C., Terray, P., Masson, S., Boschat, G., and Izumo, T.: Oceanic factors controlling the Indian summer monsoon onset in a coupled model, Clim. Dynam., doi:10.1007/s00382-014-2200-y, in press, 2014.

RanjanNayak, D., Mahapatra, A., and Mishra, P.: A survey on rainfall prediction using Artificial Neural Network, Int. J. Comput. Appl., 72, 32–40, doi:10.5120/12580-9217, 2013.

Rehfeld, K., Marwan, N., Breitenbach, S. F. M., and Kurths, J.: Late Holocene Asian summer monsoon dynamics from small but complex networks of paleoclimate data, Clim. Dynam., 41, 3–19, doi:10.1007/s00382-012-1448-3, 2013.

Romatschke, U., Medina, S., and Houze, R. A.: Regional, seasonal, and diurnal variations of extreme convection in the South Asian Region, J. Climate, 23, 419–439, doi:10.1175/2009JCLI3140.1, 2010.

ESDD
5, 1275–1317, 2014

Sankar, S., Kumar, M. R. R., and Reason, C.: On the relative roles of El Nino and Indian Ocean Dipole events on the monsoon onset over Kerala, Theor. Appl. Climatol., 103, 359–374, doi:10.1007/s00704-010-0306-7, 2011.
Sauter, T. and Venema, V.: Natural three-dimensional predictor domains for statistical precipitation downscaling, J. Climate, 24, 6132–6145, doi:10.1175/2011JCLI4155.1, 2011.
Sauter, T., Schneider, C., Kilian, R., and Moritz, M.: Simulation and analysis of runoff from a partly glaciated meso-scale catchment area in Patagonia using an artificial neural network, Hydrol. Process., 23, 1019–1030, doi:10.1002/hyp.7210, 2009.
Schönwiese, C.-D., Walter, A., and Brinckmann, S.: Statistical assessments of anthropogenic and natural global climate forcing. An update, Meteorol. Z., 19, 3–10, doi:10.1127/0941-2948/2010/0421, 2010.
Schoof, J. T.: Statistical downscaling in climatology, Geogr. Compass, 7, 249–265, doi:10.1111/gec3.12036, 2013.
Schoof, J. T. and Pryor, S. C.: Downscaling temperature and precipitation: a comparison of regression-based methods and Artificial Neural Networks, Int. J. Climatol., 21, 773–790, doi:10.1002/joc.655, 2001.
Shrestha, D., Singh, P., and Nakamura, K.: Spatiotemporal variation of rainfall over the central Himalayan region revealed by TRMM precipitation radar, J. Geophys. Res., 117, D22106, doi:10.1029/2012JD018140, 2012.
Shrestha, M. L.: Interannual variation of summer monsoon rainfall over Nepal and its relation to Southern Oscillation Index, Meteorol. Atmos. Phys., 75, 21–28, doi:10.1007/s007030070012, 2000.
Shukla, R. P., Tripathi, K. C., Pandey, A. C., and Das, I. M. L.: Prediction of Indian summer monsoon rainfall using Niño indices: a neural network approach, Atmos. Res., 102, 99–109, doi:10.1016/j.atmosres.2011.06.013, 2011.
Sigdel, M. and Ikeda, M.: Summer monsoon rainfall over Nepal related with large-scale atmospheric circulations, J. Earth Sci. Clim. Change, 3, 112–117, doi:10.4172/2157-7617.1000112, 2012.
Singh, P. and Borah, B.: Indian summer monsoon rainfall prediction using artificial neural network, Stoch. Env. Res. Risk A., 27, 1585–1599, doi:10.1007/s00477-013-0695-0, 2013.
Slingo, J. M. and Annamalai, H.: 1997: The El Niño of the century and the response of the Indian Summer Monsoon, Mon. Weather Rev., 128, 1778–1797, doi:10.1175/1520-0493(2000)128<1778:TENOOT>2.0.CO;2, 2000.

ESDD
5, 1275–1317, 2014

Suprit, K. and Shankar, D.: Resolving orographic rainfall on the Indian west coast, Int. J. Climatol., 28, 643–657, doi:10.1002/joc.1566, 2008.
Tomassetti, B., Verdecchia, M., and Giorgi, F.: NN5: A neural network based approach for the downscaling of precipitation fields – model description and preliminary results, J. Hydrol., 367, 14–26, doi:10.1016/j.jhydrol.2008.12.017, 2009.
Wang, A. and Zeng, X.: Evaluation of multireanalysis products with in situ observations over the Tibetan Plateau, J. Geophys. Res., 117, D05102, doi:10.1029/2011JD016553, 2012.
Wang, D., Xie, Q., Du, Y., Wang, W., and Chen, J.: The 1997–1998 warm event in the South China Sea, Chinese Sci. Bull., 47, 1221–1227, doi:10.1007/BF02907614, 2002.
Wang, H. and He, S.: Weakening relationship between East Asian winter monsoon and ENSO after mid-1970s, Chinese Sci. Bull., 57, 3535–3540, doi:10.1007/s11434-012-5285-x, 2012.
Wingo, M. T. and Cecil, D. J.: Effects of vertical wind shear on tropical cyclone precipitation, Mon. Weather Rev., 138, 645–662, doi:10.1175/2009MWR2921.1, 2009.
Wulf, H., Bookhagen, B., and Scherler, D.: Seasonal precipitation gradients and their impact on fluvial sediment flux in the Northwest Himalaya, Geomorphology, 118, 13–21, doi:10.1016/j.geomorph.2009.12.003, 2010.
Xu, Z. X., Chen, Y. N., and Li, J. Y.: Impact of climate change on water resources in the Tarim River basin, Water Resour. Manage., 18, 439–458, 2004.

ESDD
5, 1275–1317, 2014

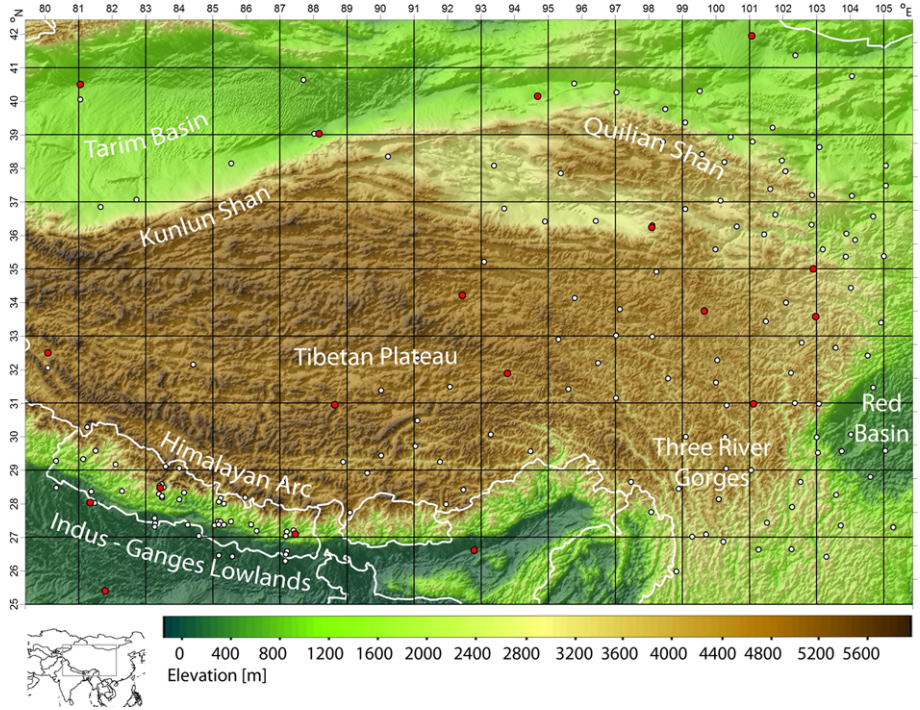

Figure 1. The target area and its main geomorphological features. The white dots indicate the locations of meteorological stations used for the implementation of the statistical downscaling model. The locations marked in red were used for the model evaluation.

ESDD
5, 1275–1317, 2014

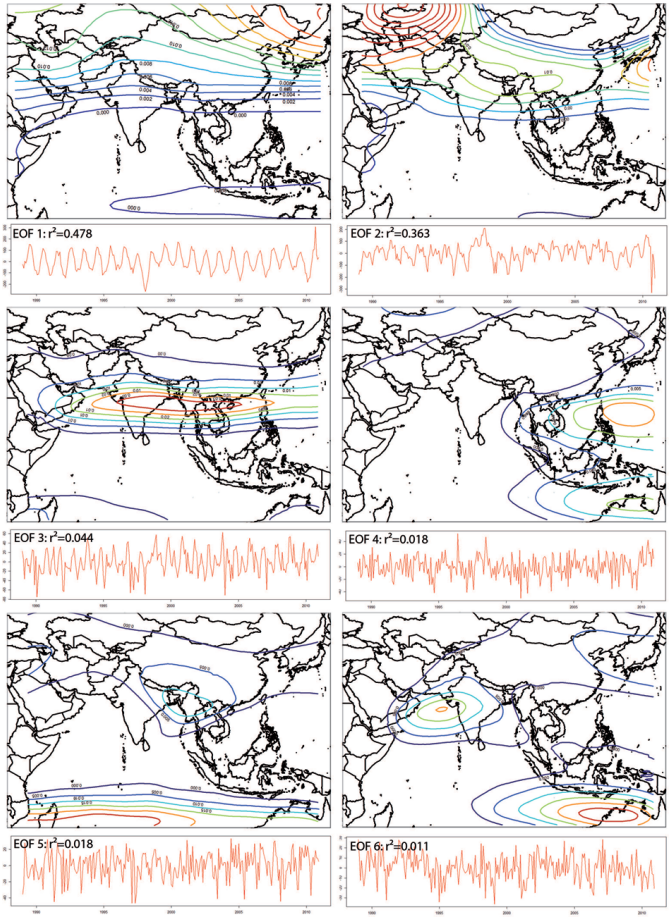

Figure 2. Spatial modes and time series of scores for the first 6 EOFs of the 500 hPa GPH anomaly over the macrogeographical region. Blue lines indicate low, red lines high values of the particular EOF.

ESDD
5, 1275–1317, 2014

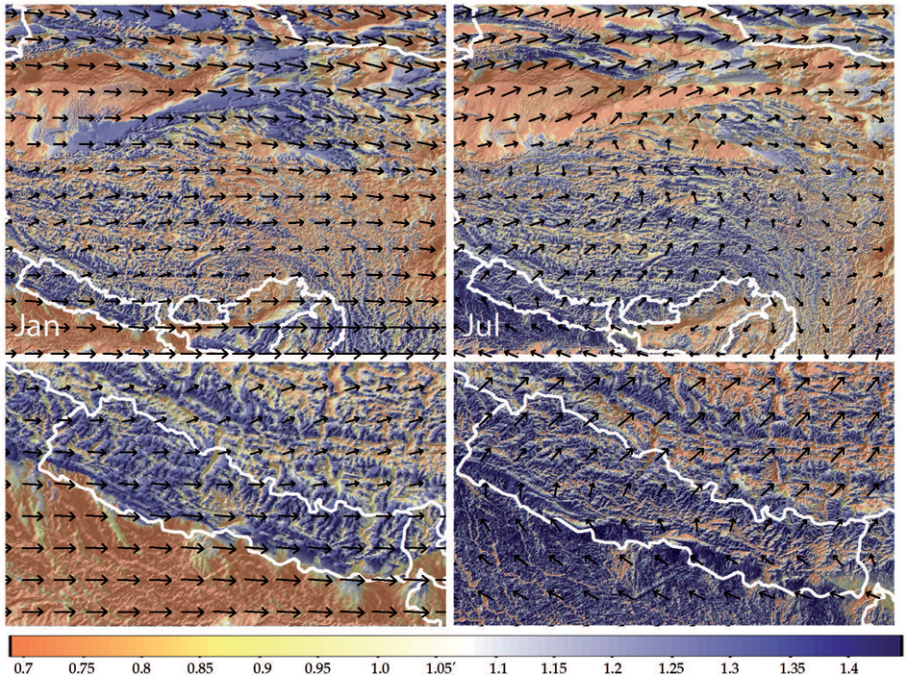

Figure 3. The spatial distribution of the wind effect parameter for January and July 2010. The arrows represent the 500 hPa ERA-Interim wind field.

ESDD
5, 1275–1317, 2014

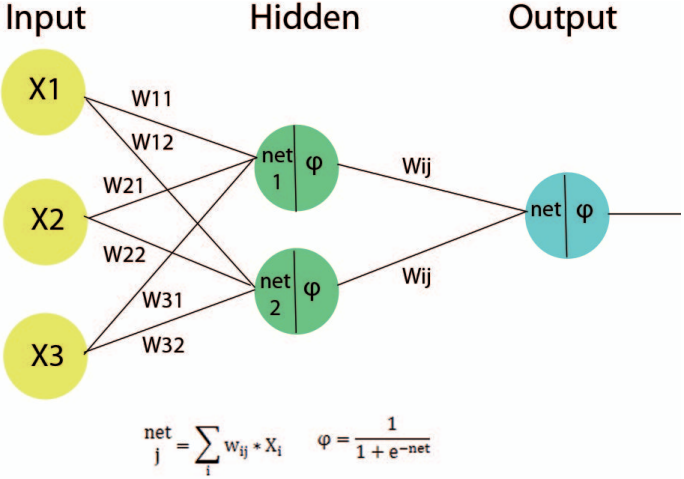

Figure 4. Schematic structure of a feed-forward artificial neural network model and the equations for the integration function net_j and the activation function φ.

ESDD
5, 1275–1317, 2014

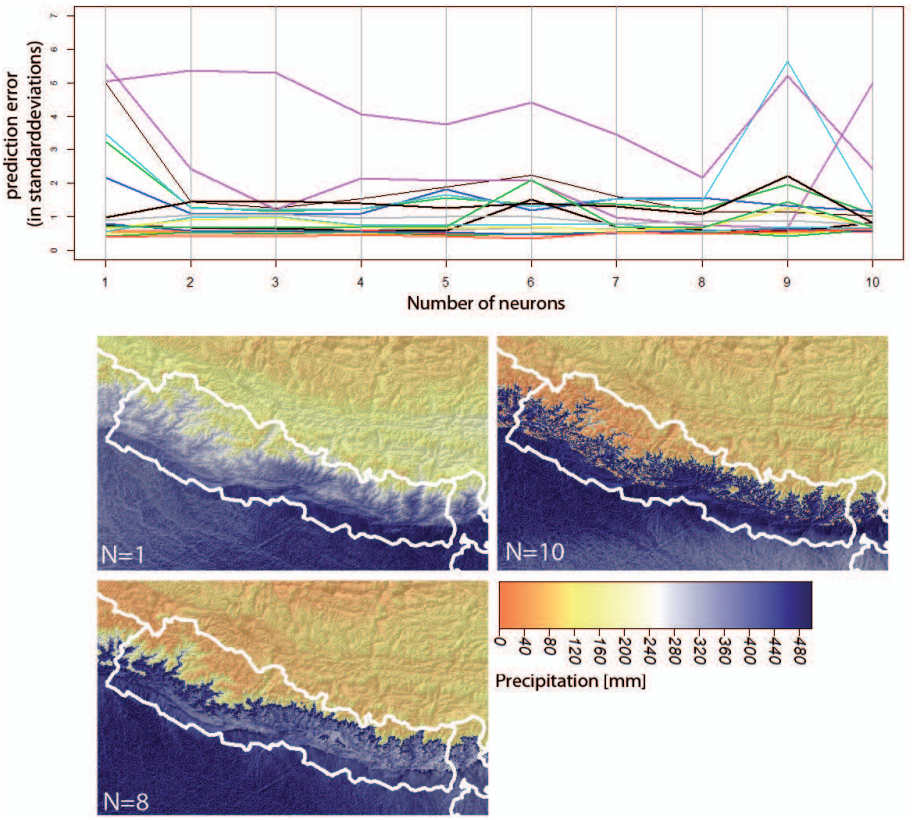

Figure 5. Normalized prediction error of various ANN architectures for 18 independent observational records (top panel) and the modeled distribution of precipitation sums for July 2010 over Nepal based on ANN architectures with N = 1, N = 8 and N = 10 neurons.

ESDD
5, 1275–1317, 2014

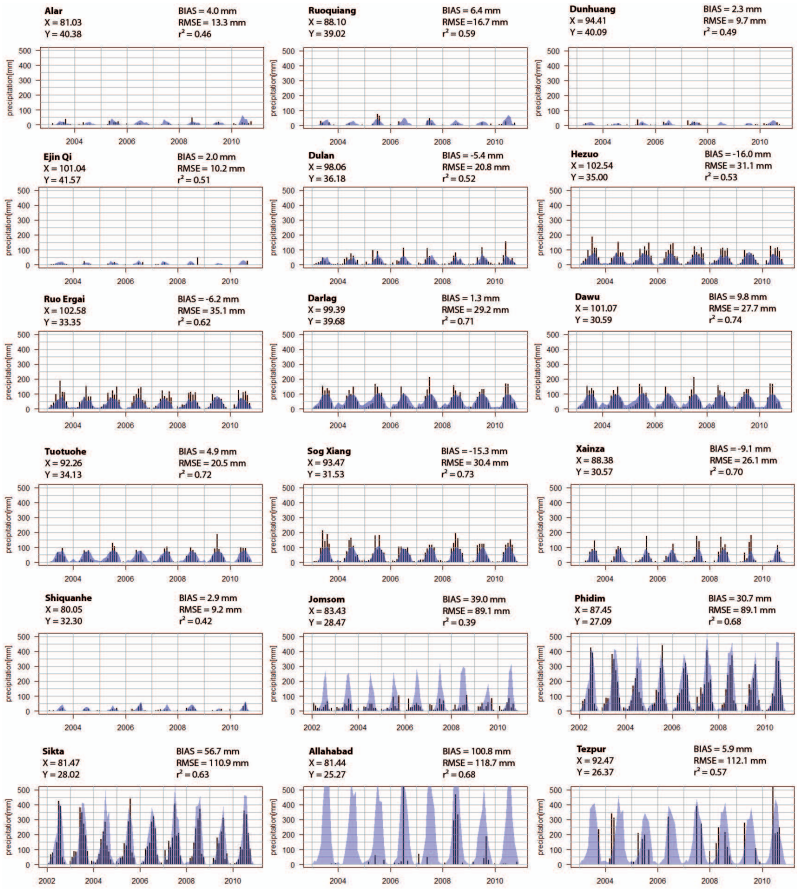

Figure 6. Observed (black bars) and modeled (polygons) monthly precipitation sums for 18 independent stations. (For the stations Allahabad and Tezpur the time series of observation exhibit conspicuous gaps.)

ESDD
5, 1275–1317, 2014

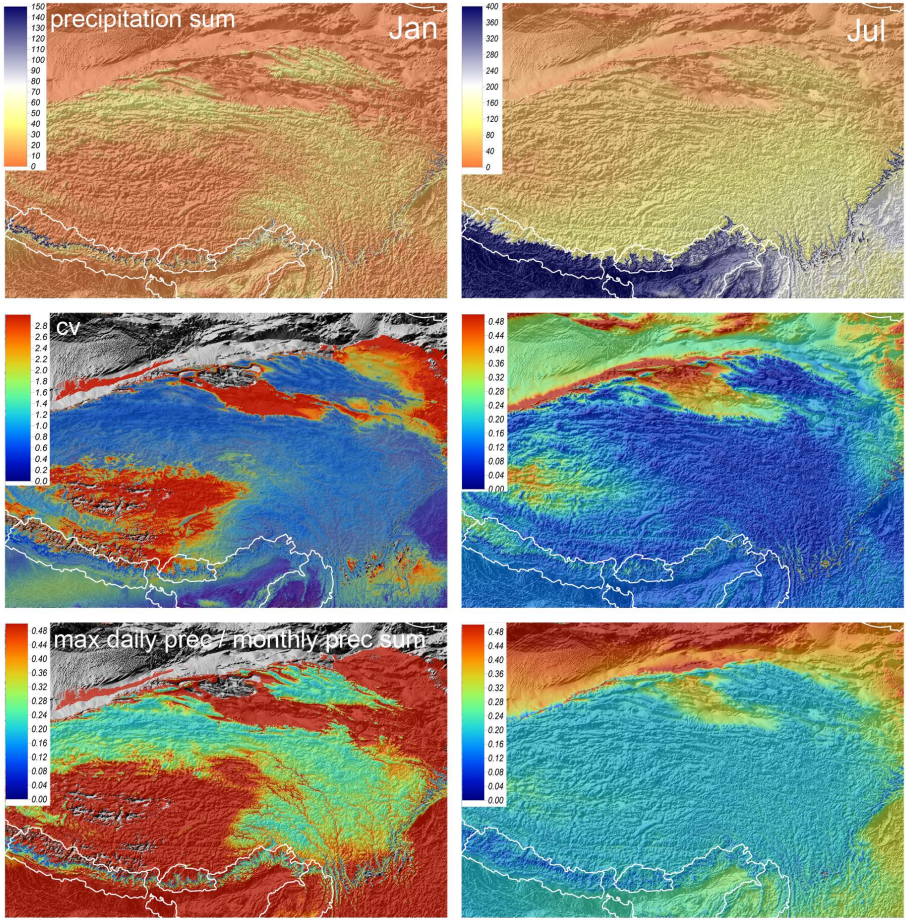

Figure 7. Mean monthly precipitation sum [mm] (top panels), coefficient of variation (middle panels) and the ratio of maximum daily precipitation and the monthly sum (bottom panels) for January (left panels) and July (right panels).

ESDD
5, 1275–1317, 2014

Large scale atmospheric forcing and topographic modification of precipitation rates

L. Gerlitz et al.

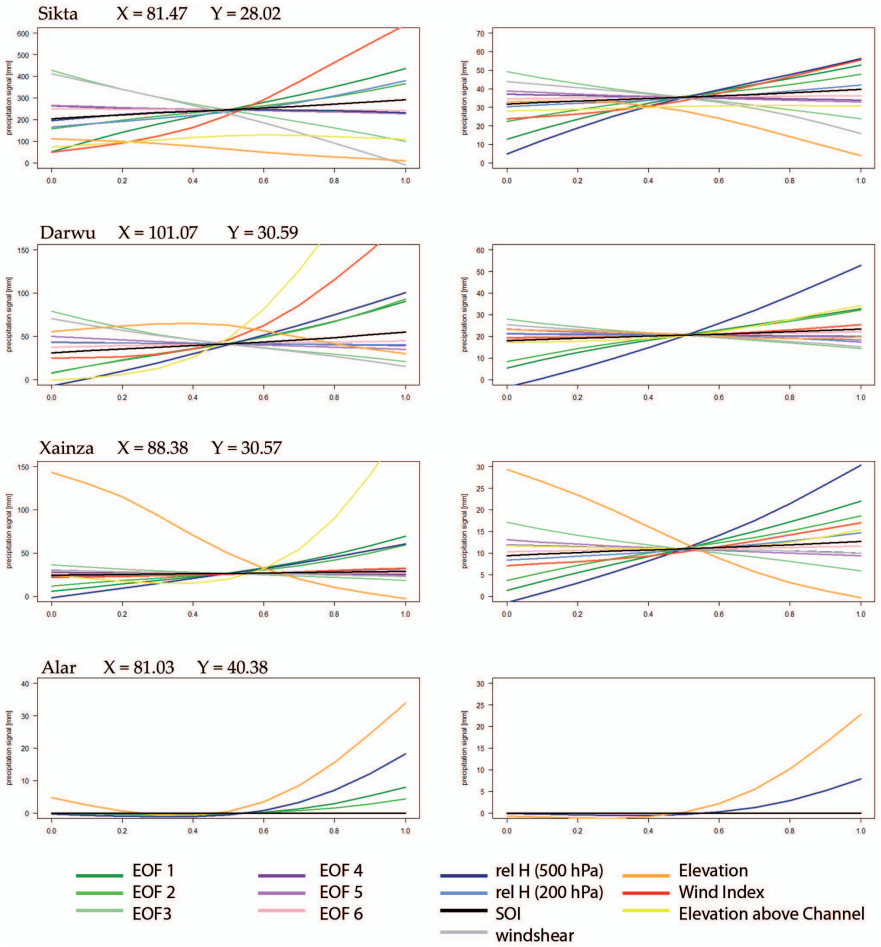

Figure 8. Sensitivity analysis of the ANN model for the atmospheric and topographic predictor variables.

ESDD
5, 1275–1317, 2014